



Time-resolved impedance spectroscopy analysis of aging in sulfide-based all-solid-state battery full-cells using distribution of relaxation times technique

Chan-Yeop Yu ^{a,*}, Junbin Choi ^b, Joshua Dunham ^a, Raziyeh Ghahremani ^a, Kewei Liu ^a, Paul Lindemann ^a, Zaine Garver ^a, Dominic Barchiesi ^a, Rashid Farahati ^a, Jung-Hyun Kim ^{b,**}

^a Corporate Competence Center – America, Schaeffler Transmission Systems LLC, Wooster, OH, 44691, USA

^b Department of Mechanical and Aerospace Engineering, The Ohio State University, Columbus, OH, 43210, USA



HIGHLIGHTS

- EIS coupled with DRT offers non-destructive analysis of all-solid-state batteries.
- Identified impedance sources of NMC/Li₆PS₅X (X = Cl, Br)/graphite full-cells.
- EIS – DRT combination thoroughly elucidate the degradation mechanisms.

ARTICLE INFO

Keywords:

Electrochemical impedance spectroscopy (EIS)
Distributions of relaxation times (DRT)
technique
All-solid-state batteries
Sulfide-based argyrodite solid electrolyte
Cell-level analysis

ABSTRACT

Electrochemical impedance spectroscopy (EIS) is a useful non-destructive technique for investigations of various electrochemical systems, including batteries. Although EIS provides abundant information over cell performance, its interpretation is often found to be challenging due to overlapping of time constants. To address the complexity and better understand the battery cell behaviors, the distributions of relaxation times (DRT) technique is employed, which facilitates deconvolutions of the frequency domains. In this study, DRT analysis was conducted to understand the electrochemical responses of all-solid-state battery full-cells made with argyrodite Li₆PS₅X (where X = Cl and Br) electrolyte. Through DRT analysis accompanied by EIS, we effectively identified and quantified the impedance sources of the full-cells. Both cathode/solid-electrolyte and anode/solid-electrolyte interfaces were examined, exploring various factors that govern all-solid-state battery performances, such as interface morphology, cathode coating, and external pressure. The extensive studies conducted using EIS – DRT combination thoroughly elucidate the degradation mechanisms in full-cells, while offering strategies to further develop the all-solid-state battery system for enhanced performances and stabilities.

1. Introduction

The global climate change issue has spurred consciousness toward the environment and led “zero-emission” to be an aspiring target. Governments, industries, and communities are committing to eliminate greenhouse gas (GHG) emissions and pollutants from industrial processes and so does it for the automotive industries. They are participating in fighting against climate change by embracing carbon neutrality or net-zero emissions. It is predicted that the electrification of transportation systems will be the ultimate solution. Electric vehicles

(EVs) offer promising key pathway toward achieving zero-emission by eliminating the involvement of fossil fuels.

To replace the conventional internal combustion engine (ICE) vehicles on a large scale, advanced battery technology is required. Although the conventional Li-ion battery (LIB) system is dominant in the EV battery market, it has certain limitations to overcome, one of which is safety. Solid-state Li-ion batteries (SS-LIBs) have gathering attentions as a promising alternative for a more sustainable future. Implementation of inorganic solid state electrolyte (SSE) in SS-LIB technology provides numerous benefits over the conventional LIBs, including enhanced

* Corresponding author.

** Corresponding author.

E-mail addresses: yucny@schaeffler.com (C.-Y. Yu), kim.6776@osu.edu (J.-H. Kim).

safety, improved thermal stability, and higher energy density compared to the liquid counterpart [1–3].

However, despite the promising benefits, the involvement of solid-state electrolyte in battery systems presents significant barriers to the development, particularly regarding the limited ionic conductivity. Solid electrolytes suffer from low ionic conductivity that even the most promising candidates exhibit at least one order of magnitude lower than the liquid electrolytes, hindering ion transport within the battery [2,4]. In addition to the intrinsic ionic conductivities, high electrode/electrolyte interface resistance poses an additional hurdle that is required to be processed during the assemblies. Moreover, well-constructed interface can be compromised due to the volume changes of the active materials over repeated cycles, further impacting the battery's overall performance and lifespan.

Therefore, a comprehensive understanding of the electrochemical and resistive behavior of the materials and interfaces is crucial to address these challenges. Electrochemical impedance spectroscopy (EIS) technique has emerged as a suitable option for investigating these properties. By applying and scanning sinusoidal current or voltage across a wide range of frequencies, signals can be subjected to the various resistive sources within the battery cell [5,6]. Each impedance response is associated with the specific characteristic frequency range, enabling discrete quantification of the impedance sources. While the analysis is often accompanied by equivalent circuit models (ECMs), complexities in the frequency domains may cause misinterpretation of the data. For example, overlaps of neighboring semi-circles are often mislabeled into missing features during analysis of Nyquist plots [7].

As a supplementary approach, the distribution of relaxation times (DRT) technique was introduced for clearer interpretation of EIS data. DRT was developed to deconvolute the resistive responses in EIS data and mitigate potential misinterpretations. Fig. 1 shows an example of EIS analysis, and DRT-based analysis investigating the impedance patterns of solid-state batteries. DRT method was designed to convert each

impedance source in the raw EIS data into a distinct peak of time constant and intensity, effectively separating each impedance source [8,9]. As shown in Fig. 1 (b), DRT method identified more than 3 barriers, while the resistive responses are convoluted and represented as a single flattened semi-circle in the Nyquist curve.

Recently, DRT has been employed to investigate solid-electrolyte properties, utilizing on its advantageous features. Mertens et al. [10] conducted impedance investigation of $\text{Li}_{1.3}\text{Al}_{0.3}\text{Ti}_{1.7}(\text{PO}_4)_3$, a promising NASICON-type solid electrolytes. EIS accompanied by DRT was applied to LATP solid electrolyte in order to reveal the major ion transport mechanism. Similary, Lyagaeva et al. [11] successfully deconvoluted bulk and grain-boundary responses of $\text{BaCe}_{0.9}\text{Cd}_{0.1}\text{O}_{3-\delta}$ using DRT technique. In the meantime, Choi et al. [12] investigated hybridized solid-electrolyte composites of $\text{Li}_{6.4}\text{La}_{3}\text{Zr}_{1.4}\text{Ta}_{0.6}\text{O}_{12} - \text{Li}_{2.3}\text{C}_{0.7}\text{B}_{0.3}\text{O}_3$ through EIS and DRT, exploring different ratios and factors governing the Li-ion transport in the composite electrolytes. Also, Sharifi et al. [13] investigated Ga-doping effect of $\text{Li}_{7-3x}\text{Ga}_x\text{La}_3\text{Zr}_2\text{O}_{12}$ ($x = 0, 0.2, 0.3$, and 0.4). While Ga-dopant tends to increase the material densities, it exhibited lowered grain boundary conductivities. Hori et al. [14] applied EIS – DRT combination to evaluate intrinsic properties of two sulfide solid electrolytes: $\text{Li}_{6-x}\text{PS}_{5-x}\text{Cl}_{1+x}$ (LPSBr) and $\text{Li}_{10+x}\text{Ge}_{1+x}\text{P}_{2-x}\text{S}_{12}$ (LGPS) and their compatibilities with cathode composite ($\text{LiNbO}_3 - \text{LiCoO}_2$) and anode alloy (In-Li). The analysis could successfully discretize interface resistances in the half cell configuration and identify the bottlenecks in the cell. Likewise, Wei et al. [15] examined LiNbO_3 coating effect in $\text{LiCoO}_2/\text{Li}_{5.5}\text{PS}_{4.5}\text{Cl}_{1.5}/\text{Li}-\text{In}$ all-solid-state battery configuration. Through DRT technique, cathode electrolyte interphase (CEI) was named as the major impedance source in the system and LiNbO_3 coating was revealed to provide improved Li-ion kinetics at CEI layer. These studies have showcased the valuable insights that can be obtained from DRT technique, advancing preceded analysis conducted by ECM technique.

Researchers have extensively utilized DRT analysis to estimate the intrinsic properties (bulk and grain boundary) of solid electrolyte materials and interface resistances at electrode/electrolyte configurations. However, limited studies have been reported for full-cell construction in all-solid-state devices with graphite anode. This study focuses on the interface resistance in all-solid-state battery devices employing argyrodite-type solid electrolyte: $\text{Li}_6\text{PS}_5\text{X}$ ($X = \text{Cl}$ or Br). Impedance analysis was conducted toward NMC/SSE and graphite/SSE interfaces to identify the frequency domains of resistive sources and thoroughly interpret the electrochemical behaviors of the full-cell batteries. Additionally, the application of DRT yielded valuable information such as particle size effect in the cathode/SSE interface and effect of re-compressing cycle-aged full-cells and their underlying mechanisms. Lastly, this study successfully demonstrated an extended cycle life of over 500 cycles for the NMC/graphite all-solid-state full-cell.

2. Experimental

The fabrication of the all-solid-state device involved LiNbO_3 -coated $\text{LiNi}_{0.6}\text{Mn}_{0.2}\text{Co}_{0.2}\text{O}_2$ (NMC) as the cathode active material and the graphite as the anode active material. Argyrodite-type $\text{Li}_6\text{PS}_5\text{X}$ (where $X = \text{Cl}$ and Br) was employed as the solid electrolyte layer and Li-ionic conductive ingredient for electrodes. For electrode preparation, a slurry containing NMC, $\text{Li}_6\text{PS}_5\text{X}$, Acetylene Black, and polymer binder was coated onto the Al-foil, followed by overnight drying. Similarly, the graphite electrode was fabricated by mixing with $\text{Li}_6\text{PS}_5\text{X}$, binder, and solvent, then coated onto the Cu-foil. To maintain the controlled environment and minimize moisture and air contamination, all the processes were conducted inside an Ar-filled glovebox.

The [NMC | Argyrodite-type solid electrolyte | Graphite] cells were assembled following the described procedures: 100 mg of the argyrodite-type $\text{Li}_6\text{PS}_5\text{X}$ solid electrolyte was weighed and inserted into the in-house designed cell (see Fig. S1). The solid electrolyte was then subjected to appropriate pressure, and 10 mm-diameter cut electrodes

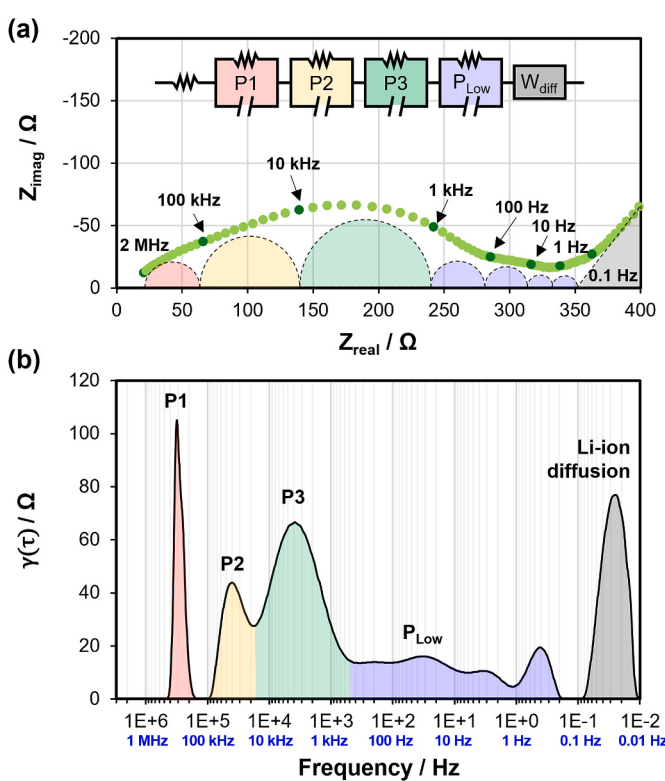


Fig. 1. Illustration of (a) electrochemical impedance spectroscopy (EIS) and (b) distributions of relaxation times (DRT) techniques, showing their application in solid-state battery research.

were attached either onto the top or bottom of the solid electrolyte pellet. For the half-cell application, the counter electrode was replaced with an indium-lithium anode. The inserted electrode/electrolyte was pelletized with high-uniaxial pressure (over 500 MPa). Subsequently, the pelletized cells were tightened to the cell fixture at a relatively low pressure of 20 MPa during the operation.

Electrochemical tests were conducted to evaluate the performance of the produced cells. Cycling tests were carried out at a C/3-rate condition (Arbin, LBT20184 battery cycler) with voltage ranges of 2.7–4.2 V for full-cell, 2.1–3.7 V for cathode half-cell, and –0.595–0.9 V for anode half-cell, respectively. EIS data was acquired in a frequency range of 2 MHz–0.1 Hz with a constant voltage of 10 mV (Gamry, Interface 5000 E). 50 % of state-of-charge (SOC) was maintained for each EIS measurement. Two different conditions were established for EIS measurements: (i) direct measurement conducted using a potentiostat, and (ii) battery cycler-driven measurement scheduled after cycle procedures. Based on the collected EIS results, DRT was computed via MATLAB-based DRT calculation code developed by T.H. Wan et al. [16].

3. Results and discussion

3.1. Identifying impedance behaviors of full-cells

Impedance growths in the sulfide-type all-solid-state batteries were observed over extended cycles for different cell configurations. Fig. 2 shows the impedance studies of full-cell, cathode half-cell, and anode half-cell. Fig. 2(a) illustrates the Nyquist plots and corresponding DRT analysis of the NMC/graphite full-cell assembled by using in-house designed pellet-die cell. The Nyquist plots of the full-cells shows two distinct semi-circles at the intermediate frequency and a straight line at low frequency domain. The first semi-circle is in the range of >50 kHz, while the second semi-circle expands from 50 kHz to 100 Hz. The second semi-circle exhibits rapid growth with increasing cycle numbers. Its corresponding DRT curves present three major peaks, labeled as P1, P2, and P3, in order of decreasing frequency. P1, located around 1.2×10^5 Hz corresponds to the first semi-circle, while P2 at ~5 kHz and P3 at ~500 Hz are associated with the second semi-circle. The P3 exhibits significant growth during cycling, in good agreement with the rapid growth observed in the second semi-circle from the Nyquist plots. This

result confirms that majority of the impedance growth was attributed to the increase of P3.

To elucidate the individual contributions of the cathode and anode interfaces, we conducted EIS and DRT analyses on NMC and graphite half-cells with the argyrodite electrolyte. In Fig. 2(b), the NMC/In-Li half-cell exhibits a similar pattern with the full-cell result. Three major DRT peaks, indexed as P1, P2, and P3, are observed, with the growth of P3 being notable. P1 (~10 kHz) corresponds to the first semi-circle, while P2 (10^4 – 10^3 Hz) and P3 (10^3 – 10^2 Hz) are assigned to the second semi-circle. The growth trend of P3 with cycle number exhibits similar behavior to that observed in the full-cell configuration. Fig. 2(c) shows graphite/Li half-cell which reveals two major DRT peaks: P1 (1.3×10^5 Hz) corresponding to high-frequency region and P2 (10^4 – 10^3 Hz) in the subsequent frequency region in their Nyquist plots. P3 is still observed in the half-cell, but its magnitude remains relatively small during cycling compared to the other DRT peaks.

The P1 and P2 are consistently observed at similar frequency regions in both the NMC/In-Li and graphite/In-Li half-cells. The P1 is considered to be (i) impedance from solid electrolyte and (ii) an artificial effect due to electrical noise or resistance from instrument set up such as cable resistances. Previous study [15] reported that the bulk and grain-boundary impedance of argyrodite solid-electrolyte (SE) can be found at the high frequency ranges. Fig. S2 shows an impedance spectrum of a simple SE acquired at low temperature of –20 °C. The simple SE cell clearly showed one ohmic impedance and one semi-circle, which is presumed as bulk and grain-boundary impedance, respectively. The semi-circle associated with grain-boundary impedance appeared at a high frequency of >100 kHz at –20 °C, and it can be identified as P1. In addition, different wire connections can create changes of resistance and inductance, which may result in P1 shifting to the high-frequency range (shown in Fig. S3). This phenomenon has also been reported by Ke et al. [17]. Both P2 and P3 are considered as interfacial impedance of each electrode since they are in the intermediate frequency ranges. The significant growth of P3 impedance was predominantly attributed to cathode, which implies that there is notable issue at the cathode-electrolyte interface.

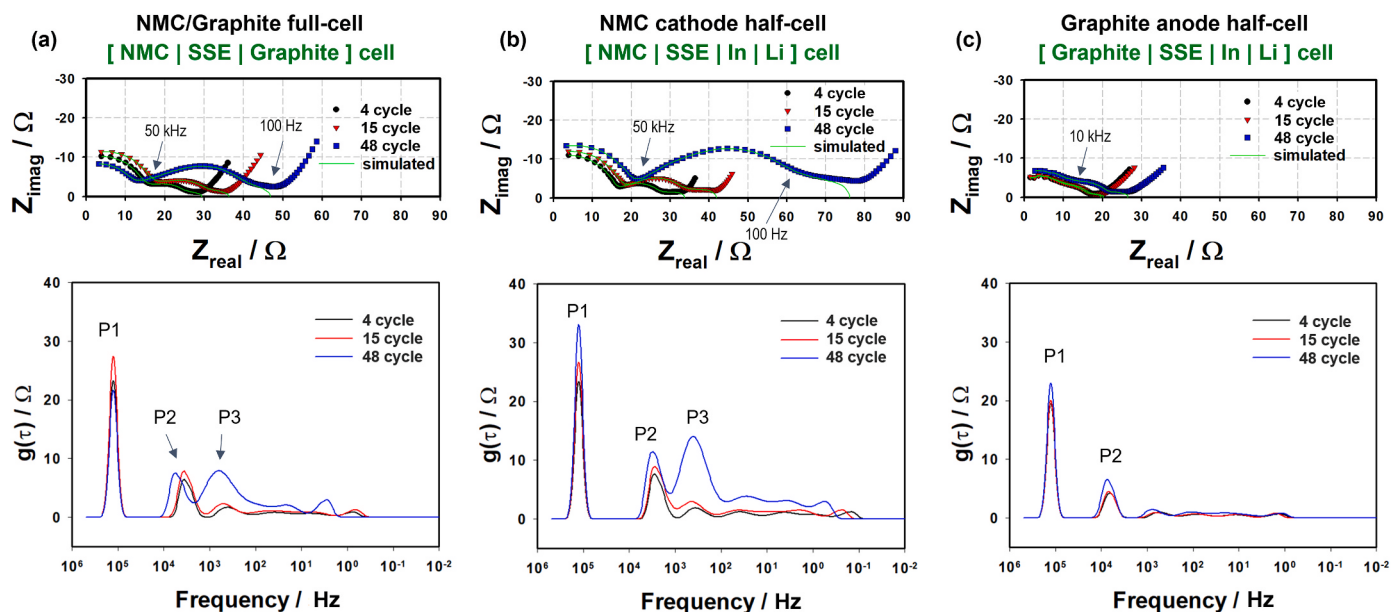


Fig. 2. Nyquist plots and corresponding DRT profiles of (a) LiNbO₃-coated NMC/graphite full-cell, (b) LiNbO₃-coated NMC/In-Li half-cell, and (c) graphite/In-Li half-cell. The DRT peaks were computed based on the simulated Nyquist curves (green solid-line) after subtracting the low-frequency data (i.e., Warburg-type diffusion). (For interpretation of the references to color in this figure legend, the reader is referred to the Web version of this article.)

3.2. Degradation on NMC cathodes

Given the significant correlation between interfacial impedance and the contact between the active material and SE, we conducted the following systematic experimental studies. To investigate the mechanical degradation between the cathode active material (CAM) and SE in cathodes, various SE sizes (nano- and micro-scale SE powders) were prepared, as depicted in Fig. 3. Previous work by P. Minnemann et al. [18] discussed the implications of particle size distribution of CAM and SE, and elaborated on their roles when varying in size. Based on this understanding, we hypothesized that using micro-sized SE for cathode fabrication could potentially result in an increased amount of voids between solid particles, which can consequently impact the cell's overall electrochemical behavior. In Fig. 3, two cells were prepared using identical procedures and conditions, but with different SE particle sizes in the cathodes only. Here, (1) the particle size of the argyrodite in electrolyte remains unchanged and (2) the cells were operated at 20 MPa pressure. The results show that changing SE from nano ($\leq 1 \mu\text{m}$) to micro-size ($\leq 20 \mu\text{m}$) in cathode can significantly affect the overall DRT signals of the cells. For instance, intensities of all the P1, P2, and P3 peaks increase when using micro-sized SE in the NMC cathode. Both cells showed the growth of P3 (10^4 - 10^3 Hz) peak intensities during cycling. In particular, the cathode with micron-sized SE exhibits a relatively rapid growth of the P3 impedance region compared to the cathode with nano-sized SE. This observation provides compelling evidence that the P3 impedance is associated with the physical contact

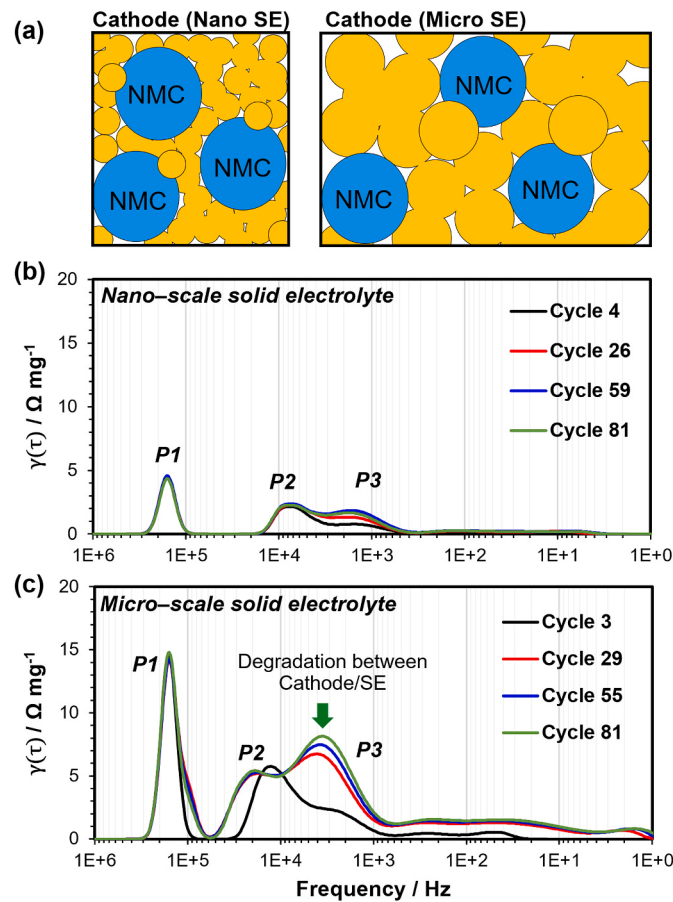


Fig. 3. (a) Schematic diagram demonstrating the impact of nano-vs. micro-sized SE particles on cathode microstructure. Assumed nano-scale SE particles provide a denser cathode (i.e., less voids) after compression ($>500 \text{ MPa}$) and deliver better mechanical contact with CAM. Evolution of DRT profiles during cycling of LiNbO₃-coated NMC/In-Li half-cells using (b) nano-scale ($\leq 1 \mu\text{m}$) and (c) micro-scale ($\leq 20 \mu\text{m}$) SEs in the cathodes.

between CAM and SE. The presence of voids between the CAM and SE can lead to non-uniform electrochemical reactions at the CAM-SE interfaces, resulting in uneven stress distribution and degradation of the contact between the CAM and SE over cycling. This analysis is consistent with previous DRT analyses on conventional Li-ion batteries, reporting the P3 impedance at similar frequency ranges (slightly above 10^3 Hz) as solid-solid contact impedance of LiFePO₄/Al and nano-Si/Cu current-collectors [19,20]. Fig. 4(a) shows that the cycle life of NMC cathodes with nano-size ($\leq 1 \mu\text{m}$) SE in half-cell at 20 MPa. It delivers discharge capacities of 171.9 mAh/g at the 1st cycle and 171 mAh/g at the 100th cycle, indicating an impressive capacity retention value of 99.5%.

Our result unambiguously demonstrates that the major degradation mode observed in the cathodes is the contact impedance growth between CAM and SE. As a next step, we attempted to rehabilitate the interfaces of over 500-times cycle-aged cells by re-compressing them at high pressures, such as 150 MPa and $>500 \text{ MPa}$. It should be noted that the operating pressures of the cells remained constant at 20 MPa regardless of the re-compression procedure. For example, the cycled cell was meticulously removed from the pressure jig to eliminate the operating pressure of 20 MPa. Subsequently, the cell was re-compressed at 150 MPa or $>500 \text{ MPa}$. Before performance measurements, the cells were compressed once again at their operating pressure of 20 MPa. In Fig. 4(b), the 500-times cycle-aged cell delivered a discharge capacity of 165 mAh/g. However, after re-compression at 150 MPa, its capacity increased to 166.9 mAh/g. When re-compressed at $>500 \text{ MPa}$, the cell capacity further improved to 173.1 mAh/g.

Fig. 4(c) and (d) show Nyquist plots and DRT profiles, respectively, of the corresponding cells after the re-compression processes. After the re-compression at 150 MPa, both the EIS and DRT analysis exhibited

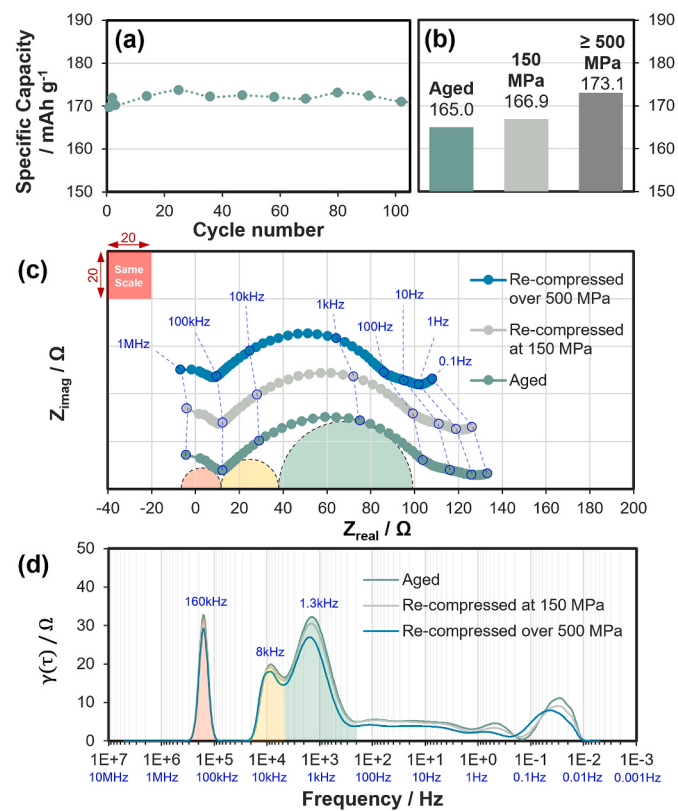


Fig. 4. (a) Cycling performance of the LiNbO₃-coated NMC cathode half-cell with operating pressure of 20 MPa. (b) Specific discharge capacities of aged half-cells before and after re-pelletizing at 150 MPa or $> 500 \text{ MPa}$. After the re-pelletizing, 20 MPa was applied to the cells as the operating pressure during cycling. The changes in (c) Nyquist plots and (d) DRT profiles before and after re-pelletizing at 150 MPa or $> 500 \text{ MPa}$.

minimal changes compared to the aged cell (i.e., prior to re-compressing). However, upon re-compressing the cell at > 500 MPa, significant changes in DRT profile were observed. Particularly discernible change was the reduction of P3 intensity with increasing re-pressurizing pressure to >500 MPa. This result reinforces the strong correlation between P3 and the mechanical contact of the CAM-SE interface. The DRT results observed during the re-compression agree with previous report by Ceder et al. [21], where a decrease in resistance in the mid-frequency range indicated a recovery of contact area as a result of external pressure. In addition, as shown in Fig. 4(b), the regeneration of interfaces through re-compression led to an increase in the specific discharge of the half-cells.

The sulfide-type SE is known to undergo a side reaction with oxide-type materials, such as NMC, due to its narrow electrochemical stability windows [22–24]. To effectively protect the CAM in contact with sulfide-based SE, LiNbO₃ coating on CAM has been demonstrated [25]. Therefore, we have used the LiNbO₃ coated cathodes in the provided data (e.g., Figs. 1–3). In the next step, we aim to investigate the impact of chemical degradation on CAM-SE interfaces through EIS and DRT profiles. To this end, we examined the coating-free (i.e., bare) NMC cathode in half-cells.

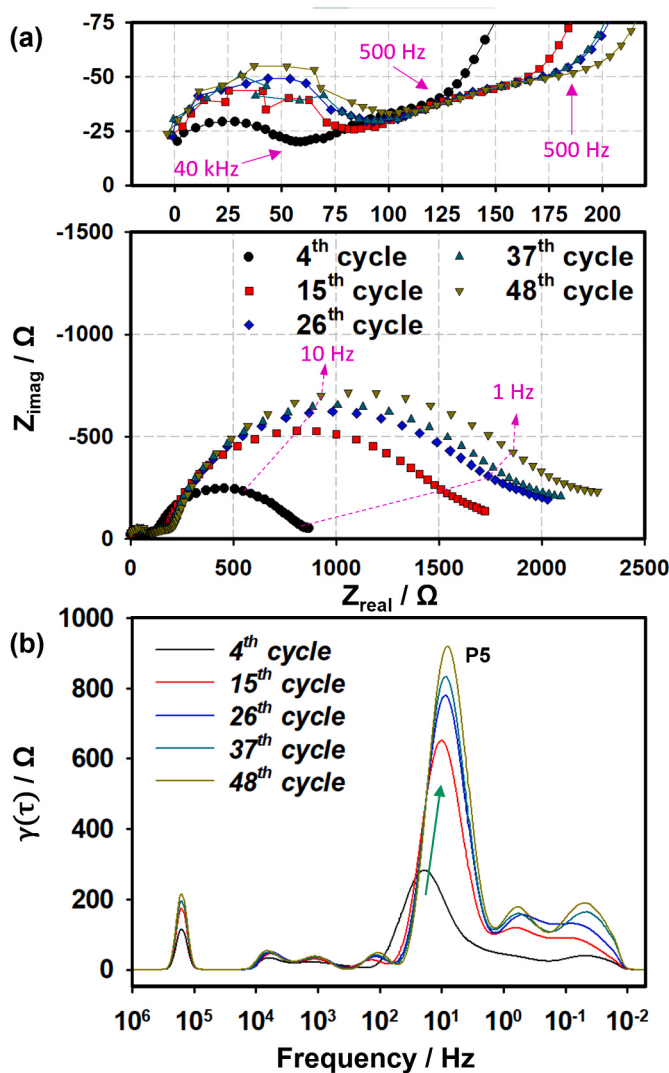


Fig. 5. (a) Nyquist plots and (b) DRT profiles of coating-free (i.e., bare) NMC cathode half-cell recorded during cycling under 20 MPa. In the Nyquist plots, the frequency changes were indexed by magenta color. (For interpretation of the references to color in this figure legend, the reader is referred to the Web version of this article.)

In Fig. 5(a), the Nyquist plots reveal a significant growth of the second semi-circle, corresponding to the low-frequency domain between 500 Hz and 1 Hz, indicating that the low-frequency impedance is influenced by the oxidative decomposition of SE. A similar trend is observed in the DRT profiles as shown in Fig. 5(b). With increasing cycle numbers, most impedance sources become enlarged, particularly P5 (at around 10 Hz) showing the most significant growth. This frequency range aligns well with charge-transfer resistance of the NMC CAM reported in literature [26,27]. The side reaction at NMC surface can lead to the formation of electrically insulating layers on the CAM, interfering the charge-transfer process. Chemical incompatibility between the sulfide electrolyte and the cathode tends to decompose into byproducts such as NiS, CoS, MnS, Li₂S, Li₃PO₄, LiP_xCl_y and LiCl [25,28]. In stark contrast, the LiNbO₃-coated NMC cathode only shows minimal charge-transfer impedance over repeated cycles, as shown in Fig. 4(d). The distinct impedance behaviors observed between the coating-free and LiNbO₃-coated NMC cathodes confirm the role of LiNbO₃ in mitigating side reactions and maintaining a facile charge transfer process at cathode surfaces. This aligns with prior studies emphasizing the beneficial impact of LiNbO₃ coatings on cathode stability and performance [15,29].

3.3. Degradation on graphite anodes

Fig. 6 illustrates the cycle life, EIS, and DRT analyses of graphite anode half-cell measured under 20 MPa. In Fig. 6(a), the graphite anode half-cell exhibits a good cycle stability, with a notably high Coulombic efficiency >99.99 %. The Nyquist plots for the graphite anode half-cell demonstrate relatively minor impedance growth over cycling. The corresponding DRT profiles reveal negligible changes in P1 – P3 (in a range of 300 kHz–200 Hz). However, P4 (in a range of 100 Hz–1 Hz), which belongs to the 2nd semicircle in the Nyquist plots, exhibits a gradual increase in peak intensity, as illustrated in Fig. 6(c). The frequency range of the 2nd semicircle is associated with the charge-transfer impedance of graphite anodes in Li-ion batteries [30].

As discussed earlier, the growth of charge-transfer impedance in the coating-free NMC cathode was attributed to the oxidative decomposition of the argyrodite solid electrolyte (SE). Similarly, at the graphite anode interface, the absence of surface coating on graphite can lead to the reduction of the argyrodite SE. Although the argyrodite SE forms a solid-electrolyte interphase (SEI) layer on the anode surface [31], the electrochemical stability of this SEI layer has not been as well-developed as it is in conventional Li-ion batteries with well-optimized electrolyte compositions, typically fortified with numerous electrolyte additives. Non-uniform thickness of the electrode, cracks, and decompositions of electrolyte are involved in ill-constructed SEI layer between the graphite anode and SE [32]. As a result, the increase in charge transfer impedance becomes a critical factor on the graphite anode side, unlike in the case of the LiNbO₃-coated NMC cathode.

In Fig. 7(a), the cycle life of the NMC/graphite full-cell is demonstrated, exhibiting an initial capacity of 192.4 mAh/g and, after the 200th cycle, the capacity reaches 179.8 mAh/g. After 500 cycles, the full-cell delivers a specific discharge capacity of 169.9 mAh/g. Similar to the half-cells, the aged full-cell underwent re-compression at > 500 MPa pressure to regenerate the electrode-SE interfaces. It is notable that the operating pressures of the full-cells remained constant at 20 MPa. As shown in Fig. 7(b), the re-compressed full-cell delivered slightly increased capacity (~1.2 %). Fig. 7(c) and (d) illustrate Nyquist plots and corresponding DRT profiles of the full-cells before (i.e., aged) and after re-compression.

The DRT peak at approximately 160 kHz, labeled as P1, corresponds to the first semi-circle, which was identified as the grain-boundary impedance of the SE. The second and third DRT peaks correspond to the second semi-circle in the Nyquist plots. The low-frequency domain (10–0.1 Hz) is identified as the charge transfer impedance region, forming a distinct arc in the EIS curve. The EIS and DRT results provide

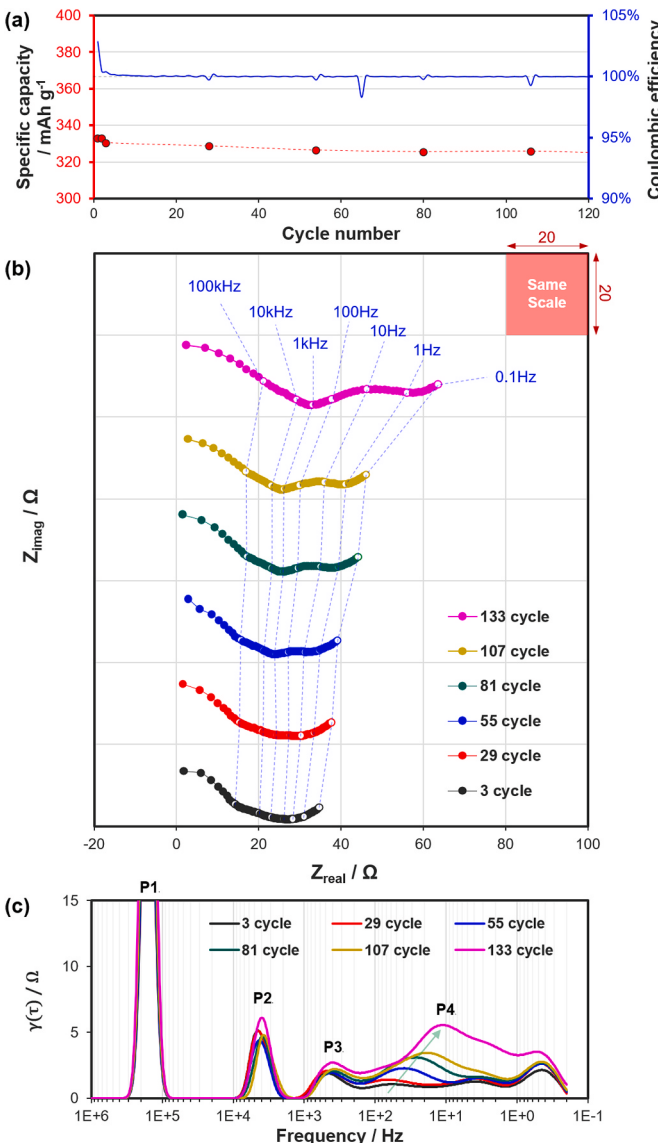


Fig. 6. (a) Specific discharge capacity and Coulombic efficiency of graphite half-cell measured under 20 MPa. (b) Evolution of (c) Nyquist plots and (d) DRT profiles of the half-cells during cycling.

compelling evidence supporting the assumption that P3 (around 1 kHz) is associated with the contact between the cathode and SE. Although the P3 peak is also present in the graphite anode, it remains stable over repeated cycles. This observation indicates that the contact impedance of the LiNbO₃-coated NMC cathode has a more significant impact on the overall impedances of the full-cell. The large charge-transfer impedance at low frequency is attributed to the graphite anode, as evidenced by the rapid growth of charge transfer impedance in the graphite anode half-cell, whereas the charge transfer impedance remained relatively stable in the cathode half-cell.

Fig. 8 and Table 1 provide a comprehensive overview of the frequency domain and the corresponding physical interpretations of individual impedances. The P1, characterized by frequencies greater than 10⁵ Hz, is assumed to encompass (i) the impedance arising from the SE and (ii) an artificial effect originating from exterior wires [33]. Variations observed in different connections can further elucidate the role of the P1.

The nature of the P2 remains to be fully elucidated, but our experimental data suggest that it may be associated with the chemical interfacial impedance at cathode and/or anode in contact with SE, such as the

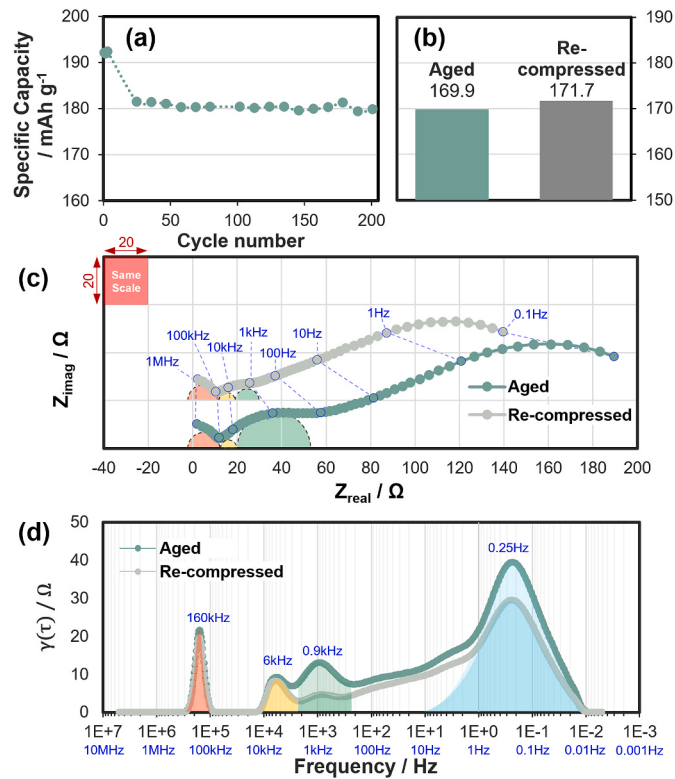


Fig. 7. (a) Cycling performance of the LiNbO₃-coated NMC/graphite full-cell under operating pressure of 20 MPa. (b) Specific discharge capacities of the aged full-cells before and after re-pelletizing at > 500 MPa. The changes in (c) Nyquist plots and (d) DRT profiles of the full-cell before and after re-pelletizing at > 500 MPa.

solid-electrolyte interphase (SEI) on graphite or cathode-electrolyte interphase (CEI) on the LiNbO₃-coated NMC cathode. Our result suggests that it would be distinguishable from the mechanical contact, which is influenced by the geometry of the cathodes and anode, as verified by examining different particle sizes of the SE in the cathode (refer to Fig. 3).

Such mechanical contact impedance between the electrode and SE is characterized as the P1 peak. The P3 peak was dominant at the cathode-SE contact with cycles and could be effectively reduced by applying re-compression to the aged half- and full-cells. The P4 (at 100 Hz–0.1 Hz) and P5 (at around 10 Hz) are considered as charge transfer impedances. P4 is observed in the anode half-cell, while P5 is noticeable from the coating-free NMC cathode in half-cell.

4. Conclusions

The primary goal of this study was to identify the characteristics of impedance sources and major degradation mechanisms, focusing on interfaces, during extended cell cycles by using EIS and DRT, as non-destructive analysis methods. To this end, we conducted systematic analysis on the electrochemical responses of LiNbO₃-coated NMC/Li₆PS₅X (where X = Cl and Br)/graphite full-cells. The comprehensive results of our investigations were meticulously organized and presented in Fig. 8 and Table 1. The chemo-mechanical evolution of interfaces at the NMC cathode and graphite anode led to the degradation of the full-cells. It is important to note that the specific values obtained from these analyses may vary depending on factors such as the materials selection, manufacturing processes, and testing conditions. Regardless of these variables, it is imperative to maintain a good interface during cell fabrication to prevent significant growth of any cell impedance; particularly P3, which represents the mechanical contact between the

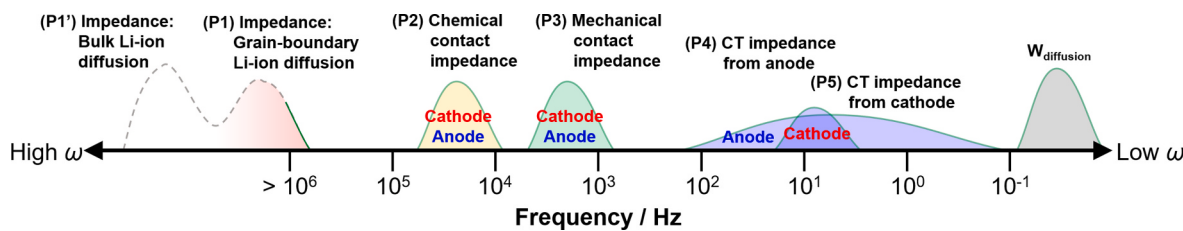


Fig. 8. Summarized interpretation of DRT peaks in sulfide-type solid-state batteries across frequency domains.

Table 1

Summary of proposed impedance sources, observed frequency ranges, and supporting experimental evidences/references in sulfide-type solid-state battery full-cells.

Label	Impedance Sources	Frequency (@ RT)	Evidence or Ref.
P1	Bulk and grain-boundary impedance from solid electrolyte, and/or artificial effect due to the cable	> 10 ⁶ Hz	Ref. (J.G. Lyagaeva et al.) Simple SE EIS (Fig. S2) Diff. Connection (Fig. S3)
P2	Chemical contact impedance: SEI and CEI	~10 ⁴ Hz	Aging mechanism (Figs. 2–7)
P3	Mechanical contact impedance of active material/SE and/or electrode/current-collector	~10 ³ Hz	Diff. Size of SE (Fig. 3) Cycling test, and re-compressing (Figs. 5–7)
P4	Charge transfer impedance: graphite anode	10 ² –10 ⁻¹ Hz	Anode half-cell cycling test (Fig. 6)
P5	Charge transfer impedance: NMC cathode/Imperfect LiNbO ₃ coating layer and CEI degradation	~10 Hz	Coating-free NMC half-cell (Fig. 4)

active material and SE. Consequently, this work can serve as a valuable reference for providing a preliminary direction in the pursuit of solid-state battery development and characterization.

Funding

The funding grant was internally funded by the Schaeffler group.

CRediT authorship contribution statement

Chan-Yeop Yu: Conceptualization, Data curation, Methodology, Project administration, Validation, Visualization, Writing – original draft, Writing – review & editing. **Junbin Choi:** Investigation, Writing – original draft, Writing – review & editing. **Joshua Dunham:** Conceptualization, Methodology, Supervision, Validation. **Raziye Ghahremani:** Conceptualization, Supervision. **Kewei Liu:** Conceptualization, Data curation, Supervision. **Paul Lindemann:** Investigation, Supervision. **Zaine Garver:** Data curation, Validation, Visualization. **Dominic Barchiesi:** Data curation, Validation. **Rashid Farahati:** Conceptualization, Project administration, Resources, Supervision. **Jung-Hyun Kim:** Conceptualization, Methodology, Project administration, Supervision, Writing – review & editing.

Declaration of competing interest

The authors declare that they have no known competing financial interests or personal relationships that could have appeared to influence the work reported in this paper.

Data availability

The authors do not have permission to share data.

Appendix A. Supplementary data

Supplementary data to this article can be found online at <https://doi.org/10.1016/j.jpowsour.2024.234116>.

References

- [1] A. Mørchhale, Z. Tang, C. Yu, R. Farahati, J.-H. Kim, Coating materials and processes for cathodes in sulfide-based all solid-state batteries, *Curr. Opin. Electrochem.* 39 (2023) 101251, <https://doi.org/10.1016/j.coelec.2023.101251>.
- [2] A. Manthiram, X. Yu, S. Wang, Lithium battery chemistries enabled by solid-state electrolytes, *Nat. Rev. Mater.* 2 (2017), <https://doi.org/10.1038/natrevmats.2016.103>.
- [3] M.V. Reddy, C.M. Julien, A. Mauger, K. Zaghib, Sulfide and oxide inorganic solid electrolytes for all-solid-state Li batteries: a review, *Nanomaterials* 10 (2020) 1606, <https://doi.org/10.3390/nano10081606>.
- [4] C. Li, Z. Wang, Z. He, Y. Li, J. Mao, K. Dai, C. Yan, J. Zheng, An advance review of solid-state battery: challenges, progress and prospects, *Sustain. Mater. Techno.* 29 (2021) e00297, <https://doi.org/10.1016/j.susmat.2021.e00297>.
- [5] J.R. Macdonald, W.B. Johnson, Fundamentals of impedance spectroscopy, in: *Impedance Spectroscopy*, John Wiley & Sons, Ltd, 2018, pp. 1–20, <https://doi.org/10.1002/9781119381860.ch1>.
- [6] A. Lasia, Electrochemical impedance spectroscopy and its applications, in: B. E. Conway, J.O. Bockris, R.E. White (Eds.), *Modern Aspects of Electrochemistry*, Springer US, Boston, MA, 2002, pp. 143–248, https://doi.org/10.1007/0-306-46916-2_2.
- [7] M. Gabersček, Understanding Li-based battery materials via electrochemical impedance spectroscopy, *Nat. Commun.* 12 (2021) 6513, <https://doi.org/10.1038/s41467-021-26894-5>.
- [8] P. Vadhra, J. Hu, M.J. Johnson, R. Stocker, M. Braglia, D.J.L. Brett, A.J.E. Rettie, Electrochemical impedance spectroscopy for all-solid-state batteries: theory, methods and future outlook, *Chemelectrochem* 8 (2021) 1930–1947, <https://doi.org/10.1002/celec.202100108>.
- [9] J. Illig, M. Ender, T. Chrobak, J.P. Schmidt, D. Klotz, E. Ivers-Tiffée, Separation of charge transfer and contact resistance in LiFePO₄-cathodes by impedance modeling, *J. Electrochem. Soc.* 159 (2012) A952–A960, <https://doi.org/10.1149/2.030207jes>.
- [10] A. Mertens, S. Yu, N. Schön, D.C. Gunduz, H. Tempel, R. Schierholz, F. Hausen, H. Kunigl, J. Granwehr, R.-A. Eichel, Superionic bulk conductivity in Li_{1.3}Al_{0.3}Ti_{1.7}(PO₄)₃ solid electrolyte, *Solid State Ionics* 309 (2017) 180–186, <https://doi.org/10.1016/j.ssi.2017.07.023>.
- [11] J.G. Lyagaeva, G.K. Vdovin, D.A. Medvedev, Distinguishing bulk and grain boundary transport of a proton-conducting electrolyte by combining equivalent circuit scheme and distribution of relaxation times analyses, *J. Phys. Chem. C* 123 (2019) 21993–21997, <https://doi.org/10.1021/acs.jpcc.9b05705>.
- [12] J. Choi, J.-H. Kim, Composition - structure - Property relationship of Li₂3C_{0.7}BO₃ – Li₆4La₃Zr_{1.4}Ta_{0.6}O₁₂ for composite cathodes in all solid-state batteries, *Solid State Ionics* 378 (2022) 115900, <https://doi.org/10.1016/j.ssi.2022.115900>.
- [13] O. Sharifi, M. Golmohammad, M. Soozandeh, A.S. Mehranjani, Improved Ga-doped Li₇La₃Zr₂O₁₂ garnet-type solid electrolytes for solid-state Li-ion batteries, *J. Solid State Electrochem.* (2023), <https://doi.org/10.1007/s10008-023-05522-w>.
- [14] S. Hori, R. Kanno, X. Sun, S. Song, M. Hirayama, B. Hauck, M. Dippon, S. Dierickx, E. Ivers-Tiffée, Understanding the impedance spectra of all-solid-state lithium battery cells with sulfide superionic conductors, *J. Power Sources* 556 (2023) 232450, <https://doi.org/10.1016/j.jpowsour.2022.232450>.
- [15] C. Wei, C. Yu, S. Chen, S. Chen, L. Peng, Y. Wu, S. Li, S. Cheng, J. Xie, Unraveling the LiNbO₃ coating layer on battery performances of lithium argyrodite-based all-solid-state batteries under different cut-off voltages, *Electrochim. Acta* 438 (2023) 141545, <https://doi.org/10.1016/j.electacta.2022.141545>.
- [16] T.H. Wan, M. Saccoccia, C. Chen, F. Ciucci, Influence of the discretization methods on the distribution of relaxation times deconvolution: implementing radial basis functions with DRTtools, *Electrochim. Acta* 184 (2015) 483–499, <https://doi.org/10.1016/j.electacta.2015.09.097>.

- [17] K. Pan, F. Zou, M. Canova, Y. Zhu, J.-H. Kim, Comprehensive electrochemical impedance spectroscopy study of Si-Based anodes using distribution of relaxation times analysis, *J. Power Sources* 479 (2020) 229083.
- [18] P. Minnmann, F. Strauss, A. Bielefeld, R. Ruess, P. Adelhelm, S. Burkhardt, S. L. Dreyer, E. Trevisanello, H. Ehrenberg, T. Brezesinski, F.H. Richter, J. Janek, Designing cathodes and cathode active materials for solid-state batteries, *Adv. Energy Mater.* 12 (2022) 2201425, <https://doi.org/10.1002/aenm.202201425>.
- [19] J.P. Schmidt, T. Chrobak, M. Ender, J. Illig, D. Klotz, E. Ivers-Tiffée, Studies on LiFePO₄ as cathode material using impedance spectroscopy, *J. Power Sources* 196 (2011) 5342–5348, <https://doi.org/10.1016/j.jpowsour.2010.09.121>.
- [20] J.W. Yap, T. Wang, H. Cho, J.-H. Kim, Comparison of carbon-nanofiber and carbon-nanotube as conductive additives in Si anodes for high-energy lithium-ion batteries, *Electrochim. Acta* 446 (2023) 142108, <https://doi.org/10.1016/j.electacta.2023.142108>.
- [21] T. Shi, Y.-Q. Zhang, Q. Tu, Y. Wang, M.C. Scott, G. Ceder, Characterization of mechanical degradation in an all-solid-state battery cathode, *J. Mater. Chem. A* 8 (2020) 17399–17404, <https://doi.org/10.1039/D0TA06985J>.
- [22] J. Haruyama, K. Sodeyama, L. Han, K. Takada, Y. Tateyama, Space-charge layer effect at interface between oxide cathode and sulfide electrolyte in all-solid-state lithium-ion battery, *Chem. Mater.* 26 (2014) 4248–4255, <https://doi.org/10.1021/cm5016959>.
- [23] F. Walther, R. Koerver, T. Fuchs, S. Ohno, J. Sann, M. Rohnke, W.G. Zeier, J. Janek, Visualization of the interfacial decomposition of composite cathodes in argyrodite-based all-solid-state batteries using time-of-flight secondary-ion mass spectrometry, *Chem. Mater.* 31 (2019) 3745–3755, <https://doi.org/10.1021/acs.chemmater.9b00770>.
- [24] Y. Xiao, Y. Wang, S.-H. Bo, J.C. Kim, L.J. Miara, G. Ceder, Understanding interface stability in solid-state batteries, *Nat. Rev. Mater.* 5 (2020) 105–126, <https://doi.org/10.1038/s41578-019-0157-5>.
- [25] J.-U. Cho, R. Rajagopal, D.H. Yoon, Y.J. Park, K.-S. Ryu, Control of side reactions using LiNbO₃ mixed/doped solid electrolyte for enhanced sulfide-based all-solid-state batteries, *Chem. Eng. J.* 452 (2023) 138955, <https://doi.org/10.1016/j.cej.2022.138955>.
- [26] F. Nobili, F. Croce, B. Scrosati, R. Marassi, Electronic and electrochemical properties of Li_x Ni_{1-y} Co_y O₂ cathodes studied by impedance spectroscopy, *Chem. Mater.* 13 (2001) 1642–1646.
- [27] P. Shafiei Sabet, D.U. Sauer, Separation of predominant processes in electrochemical impedance spectra of lithium-ion batteries with nickel-manganese-cobalt cathodes, *J. Power Sources* 425 (2019) 121–129, <https://doi.org/10.1016/j.jpowsour.2019.03.068>.
- [28] A. Banerjee, X. Wang, C. Fang, E.A. Wu, Y.S. Meng, Interfaces and interphases in all-solid-state batteries with inorganic solid electrolytes, *Chem. Rev.* 120 (2020) 6878–6933, <https://doi.org/10.1021/acs.chemrev.0c00101>.
- [29] M. Jiang, Q. Zhang, D.L. Danilov, R.-A. Eichel, P.H.L. Notten, Formation of a stable solid-electrolyte interphase at metallic lithium anodes induced by LiNbO₃ protective layers, *ACS Appl. Energy Mater.* 4 (2021) 10333–10343, <https://doi.org/10.1021/acsma.1c02278>.
- [30] H. Nara, D. Mukoyama, T. Yokoshima, T. Momma, T. Osaka, Impedance analysis with transmission line model for reaction distribution in a pouch type lithium-ion battery by using micro reference electrode, *J. Electrochem. Soc.* 163 (2016) A434–A441, <https://doi.org/10.1149/2.0341603jes>.
- [31] S. Narayanan, U. Ulissi, J. Gibson, Y. Chart, R. Weatherup, M. Pasta, Effect of current density on the Li – Li₆PS₅Cl solid electrolyte interphase, *Chemistry* (2022), <https://doi.org/10.26434/chemrxiv-2022-9jcht>.
- [32] L. Höltchi, C.N. Borca, T. Huthwelker, F. Marone, C.M. Schlepütz, V. Pelé, C. Jordy, C. Villevieille, M.E. Kazzi, P. Novák, Performance-limiting factors of graphite in sulfide-based all-solid-state lithium-ion batteries, *Electrochim. Acta* 389 (2021) 138735, <https://doi.org/10.1016/j.electacta.2021.138735>.
- [33] M.A. Danzer, Generalized distribution of relaxation times analysis for the characterization of impedance spectra, *Batteries* 5 (2019) 53, <https://doi.org/10.3390/batteries5030053>.